

## On the Multi Scale Modeling of Textile Reinforced Concrete

B. Zastrau, I. Lepenies, M. Richter

*Textile reinforced concrete (TRC) is a composite of textile structures made of multi-filament yarns (rovings) within a cementitious matrix. Experimental investigations of textile reinforced concrete specimens show very complex failure mechanisms on different length scales. Therefore mechanical models on the micro, meso and macro scale are introduced. The paper presents an overview on a hierarchical material model of TRC on three scales – the so called Micro-Meso-Macro-Prediction-Model. While on the micro scale the individual filaments of the fiber bundles are distinguished to determine an effective roving behavior within the mesoscopic model of the cementitious bulk material with rovings as reinforcement, models on the meso scale are used to predict the macroscopic response of the composite material.*

### 1 Introduction

Textile reinforced concrete is a new kind of a cementitious composite. In contradiction to short fiber reinforced concrete the reinforcement is an open textile structure made of continuous AR-glass or carbon rovings. One of the biggest advantages of TRC is the quasi-ductile behavior after matrix cracking, which is important for applications in civil engineering. This is due to the crack bridging of the rovings and the debonding of the roving-matrix-interface.

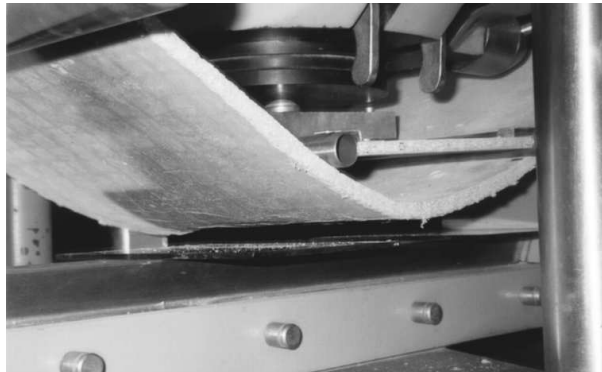


Figure 1. Textile reinforced concrete plate in 4-point-bending test  
(length  $l = 600 \text{ mm}$ , width  $w = 300 \text{ mm}$ , thickness  $t = 8 \text{ mm}$ )

Figure 1 illustrates the ductile behavior of TRC impressively, knowing that the behavior of the matrix as well as the glass yarns are very brittle by their own. The open reinforcement structure – so called lay-ups (cp. fig. 2) – is leading to a crack pattern with very small crack openings in conjunction with small crack spacings. Furthermore an optimization of the roving orientation and the roving size regarding to the expected stresses in the final structural member is possible.

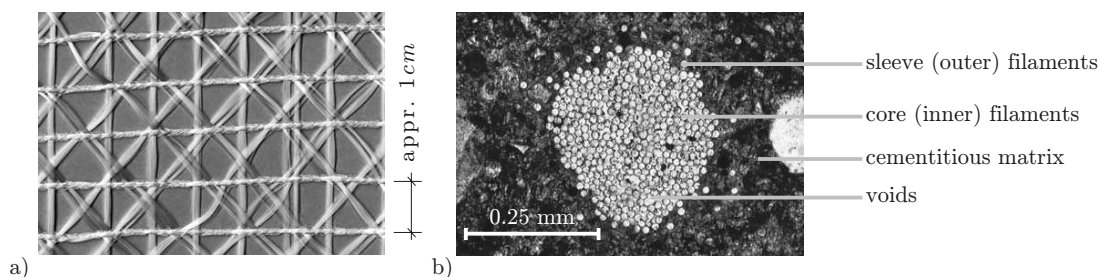


Figure 2. Textile reinforced concrete: a) multi-axial textile structure b) embedded roving (155 tex)

The behavior of TRC is characterized by complex damage and failure mechanisms on different material length scales. Beside the delamination of whole plies macroscopic matrix cracking occurs due to tension. Moreover the individual filaments of a roving can fail. Therefore a hierarchical material model is introduced [Lepenies et al. (2003); Lepenies (2007)], cp. fig. 3.

## 2 Multi Scale Analyses

Multi scale analyses (MSA) can be classified in two kinds of approaches, the hierarchical and the simultaneous MSA. Within a hierarchical MSA the model parameters of the macroscale are determined by means of homogenization associated with micromechanical field variables. Here a scale transition takes place. After the determination of effective elastic properties of the composite material no more microscopic analyses are necessary for the application of the macroscopic model.

On the other hand the simultaneous MSA – also called concurrent or integrated MSA – solves the models on all scales at the same time. Therefore the macroscopic model is affected by the response of the microscopic model and vice versa. This occurs, if a macroscopic stress redistribution takes place due to the non-linear behavior of the micro models. Hence, according to the given problem class the appropriate MSA has to be chosen.

### 2.1 A Hierarchical Multi Scale Analysis for TRC

The proposed Micro-Meso-Macro-Prediction-Model (MMM-PM) for TRC consists of three scales – the micro, the meso and the macro scale. On the micro scale the individual filaments are resolved, whereas on the meso scale only an effective roving is considered. The scale transition from the micro to the meso scale leads to an effective roving behavior. On the meso scale the multi-axial textile structure – made of rovings – is considered within the matrix. Therefore a macroscopical homogeneous material with initial and induced anisotropy has to be simulated. In order to characterize the relevant damage and failure mechanisms the bond between the reinforcement vs. matrix and the transverse matrix cracking is additionally considered on the meso scale. The aim is to predict the macroscopic behavior by means of the homogenization of the mesoscopic response of the simulated material region  $\mathcal{MR}$  or the representative volume element  $\mathcal{RVE}$ . Based on given effective strains on the macro scale appropriate boundary conditions are applied on the mesoscopic region.

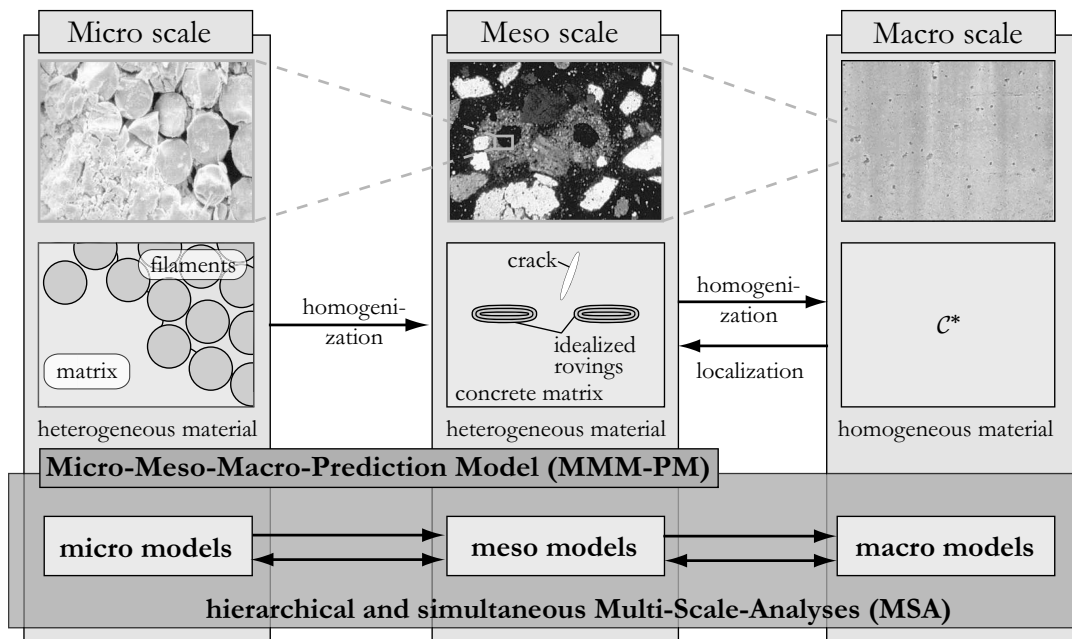


Figure 3. Idealizations of TRC on the micro, meso and macro scale

In the following we are giving a brief overview of the developed submodels of the MMM-PM on the individual scales and their interaction within the multi-scale framework. Starting with the filament bundle models on micro scale we discuss the influence of the cross sectional shape of the roving on the overall performance of TRC. On the meso scale the non-linear interaction between the reinforcement and the matrix is modeled with a slip-based

semi-analytical bond model. Here the effective roving behavior – derived from the micro model – is considered during the roving pullout after the matrix failure. Homogenization methods are developed and applied to the meso model to determine an effective behavior on the macro scale. Here an analytical homogenization model based on ESHELBY’S solution of a elastic inclusion embedded in a homogeneous matrix is used to capture the linear elastic part. The non-linear part due to the matrix cracking is modeled by means of the developed semi-analytical bond model on the meso scale.

## 2.2 TRC on the Micro Scale

Due to the small diameter of the filaments and the partial impregnation of the roving a detailed study of the load transfer mechanism on the micro scale under consideration of individual filaments and adhesive cross linkages has been investigated. Starting from detailed finite element models of the micro structure an equivalent filament bundle model (mFBM) has been developed, derived from classical fiber bundle models (FBM), cp. [Lepeniec et al. (2007)]. Classical fiber bundle models neglect the real interactions between the filaments. After failure of a single filament due to axial loading of the bundle the released stress is redistributed to the other filaments either by means of a global or a local redistribution rule. These models are quite powerful in order to get an effective response of fiber bundles without high numerical costs. Due to the shear bond between reinforcement and matrix the classical FBM is enhanced by a superposed non-uniform stress profile. Sleeve filaments are stressed more than the core filaments due to the partial impregnation of the roving with cement [Maeder and Plonka (04)]. This effect can be reduced by applying a coating to the roving, cp. fig. 4a and 4b.

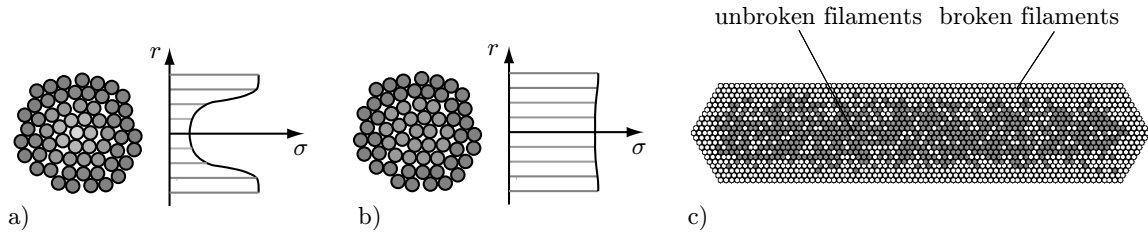


Figure 4. Stress profiles in the roving: a) uncoated b) coated rovings c) successive failure process of the roving (620 *tex*) due to filament failure

Hence the distance of a filament to the matrix affects the stress level of the filament. During the production process of TRC the loose fiber bundle changes its cross sectional shape. The cross section flattens the more filaments are combined to a roving. Therefore the aspect ratio of the bundle has to be taken into account, cp. fig. 4c.

In terms of cementitious composite engineering the stress profile is of interest to develop an optimal roving-matrix system according to the demands of application. The used FBM is based on a simple mechanical model for the individual filaments, cp. fig 5.

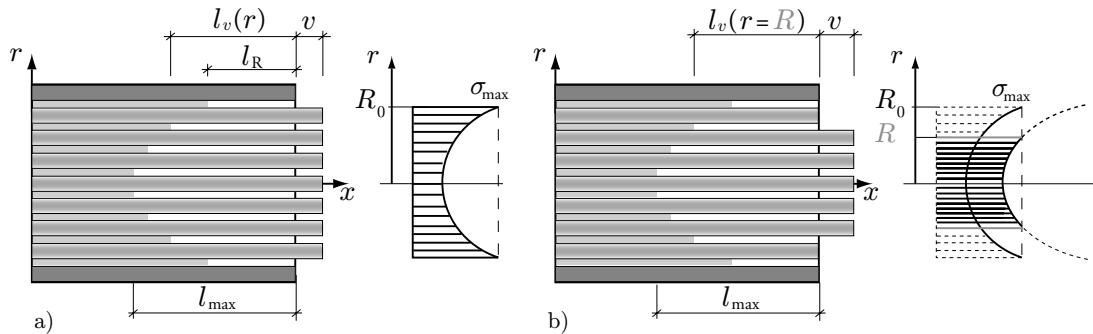


Figure 5. FBM: a) undamaged configuration b) damaged configuration

The stress of one filament  $\sigma_{fil}(r)$ ,

$$\sigma_{fil}(r) = E_{fil}\varepsilon_{fil} = E_{fil}\frac{v}{l_v(r)}, \quad (1)$$

is simply related to the assigned length  $l_v$  at the position  $r$  in the roving, where  $E_{fil}$  is the YOUNG’S modulus and  $\varepsilon_{fil}$  is the strain of the filament according the pullout displacement  $v$ . The stress profile within the roving is modeled

by means of the variation of free lengths  $l_v$  of the filaments. All filaments are stretched by the same displacement  $v$ . The overall force  $F$  due to the half crack opening displacement  $v$  is given by

$$F(v) = \int_{r=0}^R \sigma(r) dA = \int_{r=0}^R E \frac{v}{l_v(r)} dA. \quad (2)$$

The limitation on a parabolic stress profile in a circular roving leads to the analytical solution

$$F(v) = v \frac{\pi R_0^2 E}{\Delta l_v} \ln \left( \frac{l_{\max}}{l_{\max} - \Delta l_v \left( \frac{R}{R_0} \right)^2} \right), \quad (3)$$

with  $\Delta l_v = l_{\max} - l_R$ . Figure 6a shows the derived roving behavior with different stress profiles. Assuming a parabolic stress profile over the roving cross section a transition from brittle to ductile behavior is recognized, if the stress ratio  $l_{\max}/l_R$  is equal to the EULERian number  $e$ . Therefore the larger the stress difference between the core filament and the sleeve filament the more ductile the roving behaves. The amount of failed filaments within the roving increases in conjunction with a softer response of the roving. The aspect ratio of the roving cross section affects the ductile-brittle transition point TP as well, cp. fig. 6b. The roving cross section is approximated by means of superellipses, cp. section 3.

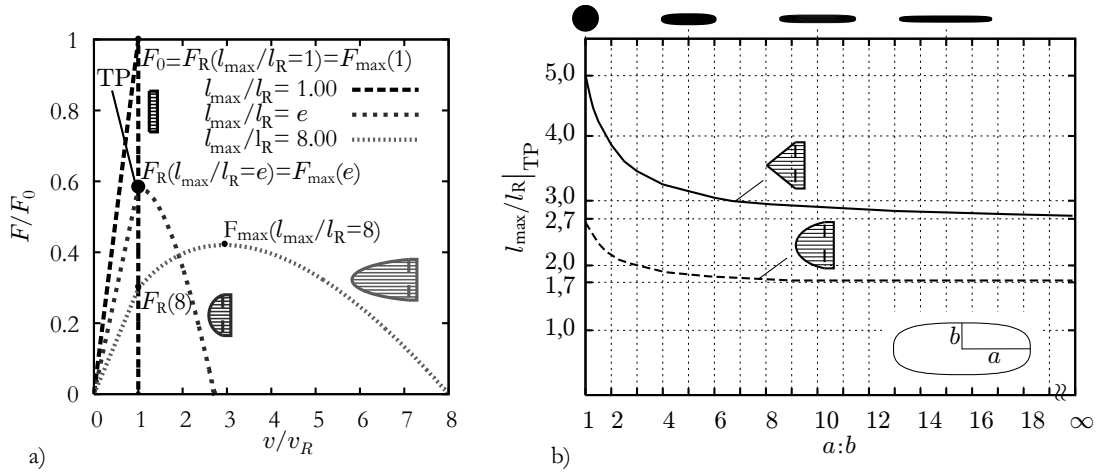


Figure 6. Theoretical roving behavior a)  $F(v)$ -relations with variation of the stress profiles b) ductile-brittle transition point TP with variation of the aspect ratio of the roving cross section

Figure 7a shows a realization  $f$  of glass filament failure stresses  $\beta_{z,fil}$ . Because of the random strength over the roving cross section according to the distribution function  $P$ , the effective roving behavior is based on 10000 FBM simulations with random property mapping. Figure 7b shows the determined mean force-strain relations ( $F(\varepsilon)$ ) for an embedded roving under tension for an assumed stress profile, roving shape and filament strength distribution exemplarily. Furthermore the damage evolution  $D_A$  of the effective roving cross section  $A_{rov}$  related to the roving strain  $\varepsilon$  is determined:

$$A_{rov}(\varepsilon) = (1 - D_A(\varepsilon)) A_{rov}^0. \quad (4)$$

This function is important in order to determine the maximal transferable bond stresses within the roving from experimental results, cp. section 4.

### 2.3 Bond Models

In order to simulate the bond behavior of the composite, the differential equation of the bond problem in eq. (5) has to be solved for the function of the slip  $s(x)$  along  $x$

$$\frac{d^2 s(x)}{dx^2} = \frac{u}{(EA)^*} \tau[s(x)], \quad (5)$$

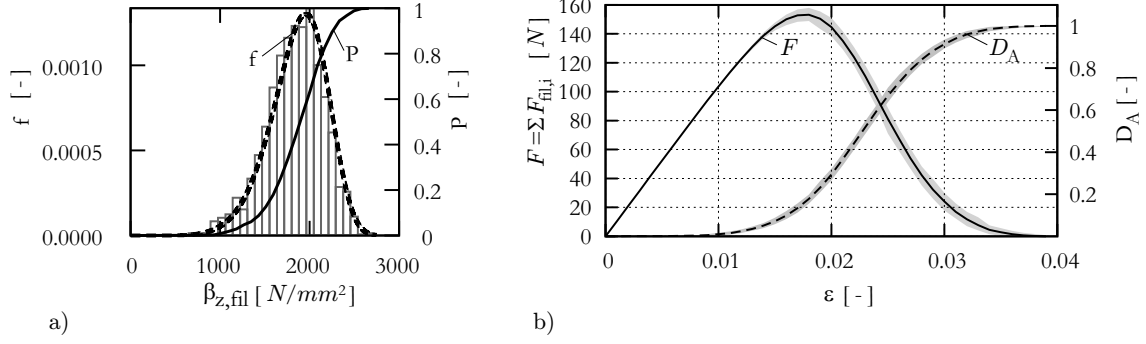


Figure 7. Effective roving behavior: a) filament strength distribution b)  $F(\varepsilon)$  and  $D_A(\varepsilon)$  relations

with the circumference  $u$  of the roving and the overall axial stiffness  $(EA)^*$ , cp. eq. (6). A so called *slip based approach* assumes a dependency of the shear stress  $\tau$  within the interface on relative displacement (slip)  $s$  of the reinforcement (index r) against the matrix (index m). The overall axial stiffness is given with

$$\frac{1}{(EA)^*} = \frac{1}{E_r A_r} + \frac{1}{E_m A_m}, \quad (6)$$

where  $E$  and  $A$  stand for the YOUNG'S modulus and the cross sectional area, respectively.

The bond relation  $\tau(s)$  depends amongst others on the mixture of the cementitious matrix, the fiber sizing and fiber coating leading to a different interface transition zone (ITZ). Thus, for each change of the system a new bond relation has to be determined. Unfortunately the interface properties are not measurable by experiments. Only a force  $F$  related to a pullout displacement  $v$  for single filament pullout tests or for roving pullout tests are available.

The bond relation can be determined indirectly from the experimental measured force-displacement relation  $F(v)$ . Often finite element analyses are used to determine the bond relation. In [Richter (2005)] a multi-linear approximation of the desired function  $\tau(s)$  is used, which leads to a piecewise analytical closed form solution of eq. (5). This avoids time intensive solutions of PDE systems. Here we are using only the solution of a piecewise constant bond law  $\tau(s)$  for small intervals  $\Delta x$  (interface length  $L = \sum_i^n \Delta x_i$ )

$$s(x) = \frac{1}{2} \frac{\tau u}{(EA)^*} x^2 + \left( \frac{N_{r,0}}{E_r A_r} - \frac{N_{m,0}}{E_m A_m} \right) x + s_0. \quad (7)$$

$N_{r,0}$  and  $N_{m,0}$  are the normal forces of the roving and the matrix at the boundary  $x = 0$  of the interval  $\Delta x$ . Starting with the boundary condition at the stress free end of the reinforcement allows for a straight forward solution of the slip distribution  $s(x)$ , the shear stress  $\tau(x)$  and normal force  $N_r(x)$  along the embedded length  $L$ , whereas the interface debonding as well as the roving pullout are considered.

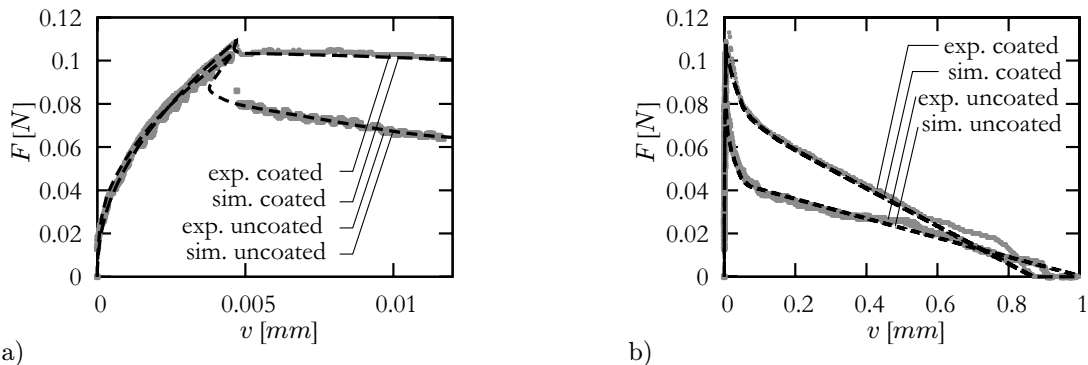


Figure 8.  $F(v)$ -relations of pullout test of uncoated and coated filaments a) detail of the debonding stage b) complete force-displacement relation

Within an optimization process the error between experimental and simulation results is minimized, to get an optimal approximation of  $\tau(s)$ . Figure 8 shows the measured and the simulated force-displacement curves of a single glass filament ( $d_f = 0.015 \text{ mm}$ ) in a pullout test ( $L = 1 \text{ mm}$ ) with different interface properties. The only unknown in eq. (5) is the bond relation  $\tau(s)$ . For an uncoated and a coated filament the identified bond laws are given in fig. 9.

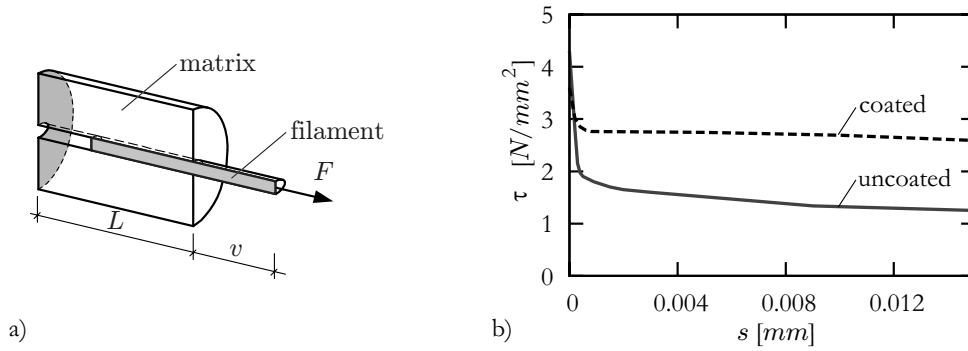


Figure 9. Pullout test a) boundary condition b) identified bond laws for uncoated and coated glass filaments in fine grained concrete matrix

The developed semi-analytical bond model works for relevant boundary conditions in terms of the available experimental setups, cp. fig. 10. A single sided pullout (fig. 10/I) of a reinforcement is characterized by a debonding stage and a final total pullout stage of the reinforcement out of the embedding matrix. In case of a so called pull through (fig. 10/II) the interface between the matrix and the reinforcement keeps constant, if the reinforcement protrudes at the unpulled end. Finally in a tension test with multiple cracks a typical boundary condition is given by a slip of zero in conjunction with a tensile force between two matrix cracks (fig. 10/III), such that there will be no displacement of the reinforcement relative to the matrix.

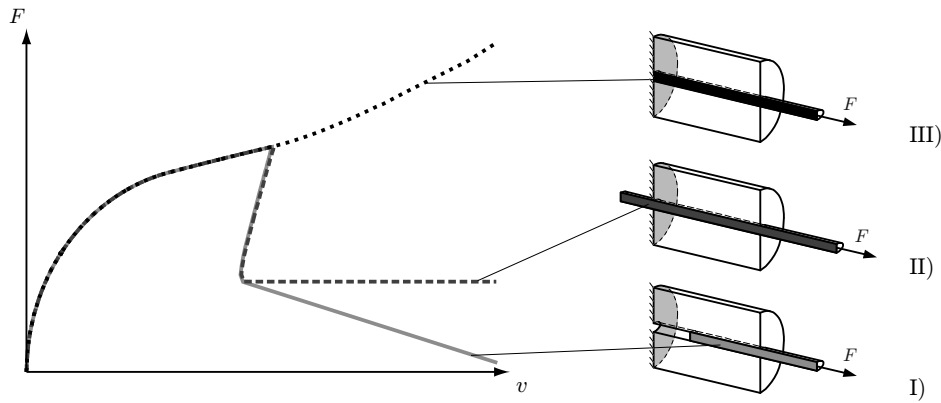


Figure 10. Different pullout boundary conditions

Prestressed rovings and pressure dependent friction laws for the interface are easily adoptable in the mechanical model. The application to pullout tests with cyclic loading demands for the implementation of damage and/or plastic material laws for all components of the composite. The presented model considers the inelastic behavior according fig. 11.

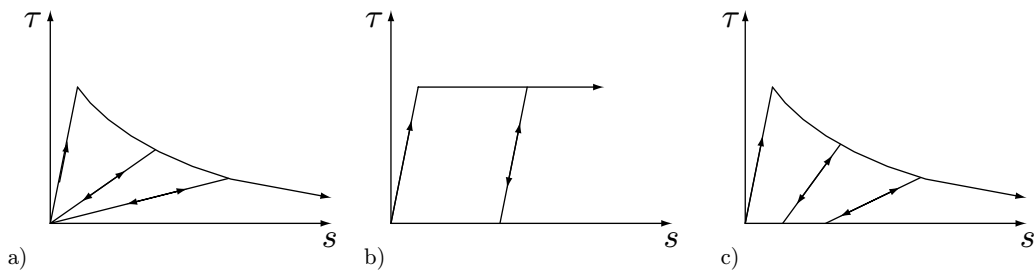


Figure 11. Bond relations: a) with damage behavior b) with elasto-plastic behavior c) with elasto-plastic damage behavior

### 3 Roving Approximation on the Meso Scale

The shape of the roving cross section is approximated by means of superellipses on the meso scale:

$$\left| \frac{x}{a} \right|^r + \left| \frac{y}{b} \right|^r = 1, \quad (8)$$

with the semi-major axis  $a$ , semi-minor axis  $b$  and the rational exponent  $r$ . The parameter  $r$  controls the angularity of the roving shape, where  $r = 2$  describes an ellipse and  $r \gg 2$  approximates a rectangle, as it is shown in fig. 12.

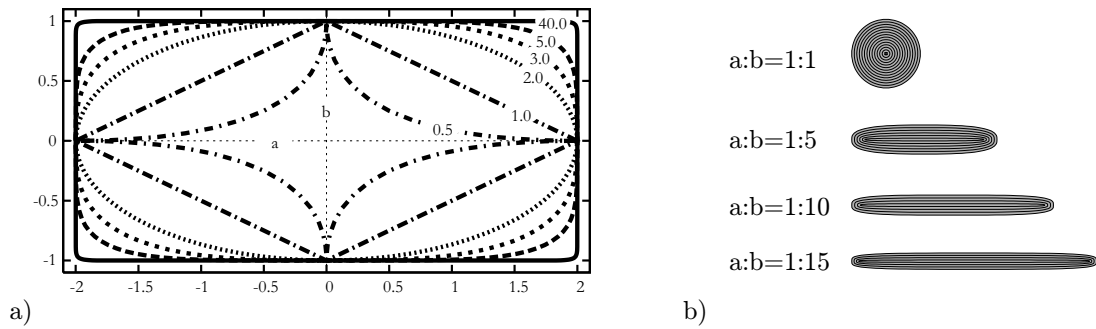


Figure 12. Approximation of roving cross sections with superellipses a) influence of the parameter  $r$  in eq. (8), b) roving cross sections

On the meso scale the successive failure of the roving is modeled on the basis of the idealized roving in fig. 13. Beside of a compact roving with an effective material law additional interfaces are considered. The uncoated roving tends to fail from the outer filaments towards the center of the roving. Furthermore, microscopic investigations of coated rovings show clusters of filaments, cp. fig. 13c and fig. 13d.



Figure 13. Idealized subdivided rovings a) compact model b) layer model c) zone model d) mixed model

#### 4 Roving Pullout

In order to model the bond behavior of fiber bundles, the effective load carrying behavior including the successive failure of the roving has to be taken into account. Due to experimental difficulties in single sided roving pullout tests a tension specimen with a single crack is considered. This double sided pullout test avoids the clamping problems of the multi filament yarn. Only the embedded length and the amount of reinforcement are different to the finally predicted tension tests with multiple matrix cracking. Up to the maximum pullout load both sides of the specimen can be treated equally like in the single sided pullout test, but the post peak behavior combines the pullout of the roving from one side with the partial pull back of the roving on the other side of the specimen. Without the knowledge of the inelastic deformation in the interface no unique solution of the pullout problem can be found, but it is possible to determine bounds assuming perfect elastic and perfect rigid bond conditions.

The longer the embedded length of the roving the more force can be transferred between the roving and the matrix. Hence, the stress in the roving will increase, which leads to a successive failure of the filaments. The stiffness of the composite gets further reduced because of the activation of weaker slip planes within the roving. Evaluating the force-strain behavior by means of the FBM in section 2.2 the determination of the bond quality within the roving is possible.

Figure 14 shows a typical force-displacement relation of a glass roving pullout test. Here the bound of a perfect elastic interface is considered. The length of the debonded roving interface  $L_{\text{debonded}}$ , i. e. that part of the interface  $L$  in which shear stresses due to occurring slip are induced, increases with increasing  $v$ . According to the micro mechanical roving simulation the reduction of the effective cross section  $A$  in eq. (4) is known. Therefore only the change of the bond quality  $\tau(s)$  in eq. (9) of the activated slip levels within the roving has to be determined:

$$\tau(s) = (1 - D_{\tau}(\varepsilon))\tau^0(s). \quad (9)$$

The reduction of the effective roving cross section is denoted with  $(1 - D_A(\varepsilon))$ , whereas the bond relation  $\tau(s)$  of an inner slip interface is related to the bond relations of the outer interface  $\tau^0(s)$  with the factor  $(1 - D_{\tau}(\varepsilon))$ . The determined functions  $D_{\tau}(\varepsilon)$  and  $D_A(\varepsilon)$  can be understood as damage functions in a framework of the damage mechanics. Here they reduce the reference shear strength and the reference cross-sectional area respectively.

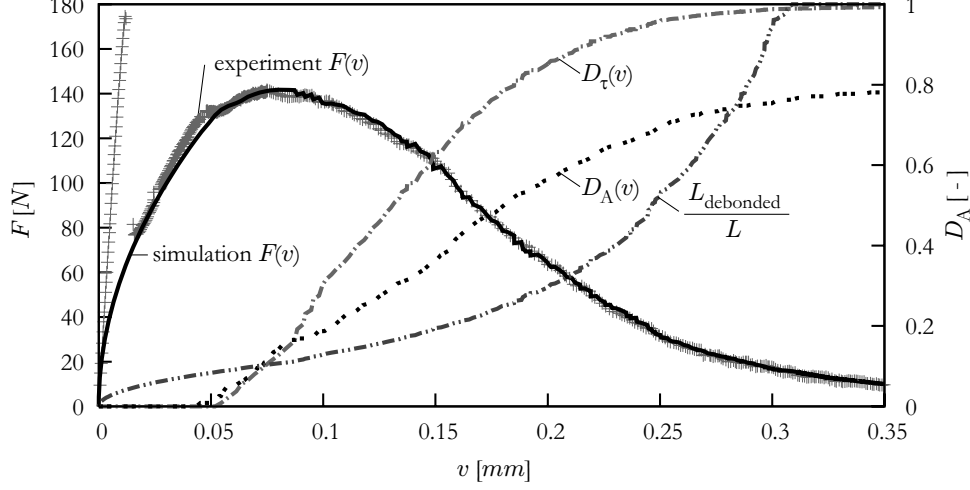


Figure 14. Pullout test of a roving: comparison between simulation and experimental data and derived damage functions

## 5 Effective Macroscopic Behavior of TRC

### 5.1 Determination of the Elastic Properties of TRC

Up to the formation of the first matrix crack the material behavior is approximately linear-elastic, but in general anisotropic, depending on the considered textile structure:

$$\langle \boldsymbol{\sigma} \rangle_{\mathcal{Y}} = \mathbf{C}^* : \langle \boldsymbol{\varepsilon} \rangle_{\mathcal{Y}}. \quad (10)$$

The volume average  $\langle \square \rangle$  of a quantity  $\square$  with respect to the domain  $\mathcal{Y}$  is defined with

$$\langle \square \rangle_{\mathcal{Y}} = \frac{1}{V} \int_{\mathcal{Y}} \square dV, \quad (11)$$

the notation  $\square^*$  denotes the equivalent coarse scale quantity of the fine scale quantity  $\square$ . The type of material symmetry and the associated independent elastic material parameters of the effective elasticity tensor  $\mathbf{C}^*$ ,

$$\mathbf{C}^* = C_{ijkl}^* \mathbf{e}_i \otimes \mathbf{e}_j \otimes \mathbf{e}_k \otimes \mathbf{e}_l \quad (12)$$

on the macro level are determined by means of analytical and numerical homogenization techniques. The macroscopic quantities are determined by subjecting the considered domain  $\mathcal{Y}$  to boundary conditions that satisfy HILLS energy conditions

$$\langle \boldsymbol{\sigma} \rangle_{\mathcal{Y}} : \langle \boldsymbol{\varepsilon} \rangle_{\mathcal{Y}} = \langle \boldsymbol{\sigma} : \boldsymbol{\varepsilon} \rangle_{\mathcal{Y}}. \quad (13)$$

Basis of the analytical homogenization is the micro-mechanical solution of the average strain in a single inclusion embedded in an elastic matrix according to [Eshelby (1957)]. In the case of ellipsoidal inclusions the strain in the inclusion is constant and with the ESHELBY tensor  $\mathbf{S}^\alpha$  of inclusion  $\alpha$  the overall elasticity tensor  $\mathbf{C}^*$  can be written as

$$\mathbf{C}^* = \mathbf{C} + \sum_{\alpha=1}^n f_\alpha ((\mathbf{C}^\alpha - \mathbf{C})^{-1} + \mathbf{S}^\alpha : \mathbf{C}^{-1})^{-1}. \quad (14)$$

Herein  $\mathbf{C}$  and  $\mathbf{C}^\alpha$  are the elasticity tensors of the concrete matrix and the textile inclusion  $\alpha$  depending on the given elastic properties of the  $n$  constituents. Further  $f_\alpha$ ,  $\alpha = \{1, 2, \dots, n\}$  are the volume fractions of the inclusions in each roving direction. This solution neglects any interaction between the inclusions and is called the dilute solution. In extension of this solution for multi-directional reinforcements an effective field approximation (EFA) is used [Mori and Tanaka (1973)]. This approach considers the interaction between the different orientated rovings in an average sense. Now the different orientated rovings  $\alpha$  are assumed to be in a matrix (volume fraction  $f_m$ ) with the still unknown average matrix strain  $\langle \boldsymbol{\varepsilon}^m \rangle$ . This problem can be solved analytically and leads to an equation for

the direct computation of the overall elasticity tensor, cp. [Richter (2005)]:

$$\mathbf{c}^* = \mathbf{c} + \sum_{\alpha=1}^n f_{\alpha} (\mathbf{c}^{\alpha} - \mathbf{c}) : \left\{ \mathbf{K}^{\alpha} + \sum_{\beta=1, \beta \neq \alpha}^n f_{\beta} (\mathbf{K}^{\beta} - f_{\beta} \mathbf{1})^{-1} : (\mathbf{K}^{\alpha} - f_{\alpha} \mathbf{1}) \right\}^{-1} \quad (15)$$

with

$$\mathbf{K}^{\alpha} = (f_m + f_{\alpha}) \mathbf{1} - f_m \mathbf{S}^{\alpha} : (\mathbf{1} - \mathbf{c}^{-1} : \mathbf{c}^{\alpha}). \quad (16)$$

The following components of the effective elasticity tensor are calculated with equation (15), assuming isotropic behavior of the textile reinforcement and the concrete matrix. In the following we considered a biaxial textile structure with 5% fiber volume fraction in each roving direction for an AR-glass-TRC and Carbon-TRC, cp. fig. 15a. Figure 15a and b show the graphical representations of the effective elasticity tensors of TRC in the cases of AR-glass and carbon reinforcements, cp. [Böhlke and Brüggemann (2001)]. The corresponding components  $\mathcal{C}_{pq}$  in VOIGT-notation are given in equations (17) and (18) ( $pq = \{11, 22, 33, 12, 13, 23\}$ ):

$$[\mathcal{C}_{pq}^*]^{\text{ARG-TRC}} = \begin{bmatrix} 36710 & 7769 & 8083 & 0 & 0 & 0 \\ 7769 & 36710 & 8083 & 0 & 0 & 0 \\ 8083 & 8083 & 35702 & 0 & 0 & 0 \\ 0 & 0 & 0 & 14294 & 0 & 0 \\ 0 & 0 & 0 & 0 & 14197 & 0 \\ 0 & 0 & 0 & 0 & 0 & 14197 \end{bmatrix} \frac{N}{mm^2}, \quad (17)$$

$$[\mathcal{C}_{pq}^*]^{\text{C-TRC}} = \begin{bmatrix} 44745 & 8069 & 8648 & 0 & 0 & 0 \\ 8069 & 44745 & 8648 & 0 & 0 & 0 \\ 8648 & 8648 & 37591 & 0 & 0 & 0 \\ 0 & 0 & 0 & 15998 & 0 & 0 \\ 0 & 0 & 0 & 0 & 15665 & 0 \\ 0 & 0 & 0 & 0 & 0 & 15665 \end{bmatrix} \frac{N}{mm^2}. \quad (18)$$

Equation (15) leads to the effective linear-elastic orthotropic elasticity tensor in the special case of biaxial roving orientations. The relative differences of the magnitudes of the components differ depending on the relative stiffness of the reinforcement. For the given fiber fraction of 5% the AR-glass structure leads to a quasi-isotropic effective elasticity tensor, whereas the carbon structure induces an anisotropy (orthotropy) with 20% difference in stiffness.

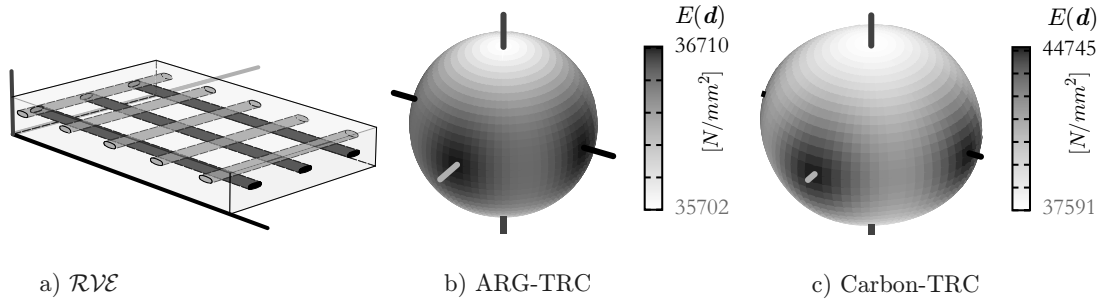


Figure 15. Graphical representation of the effective elasticity tensors of TRC a)  $\mathcal{RVE}$  with biaxial reinforcement b) AR-glass-TRC, c) Carbon-TRC

After exceeding the elastic limit of the composite first the matrix fails. Here the inelastic behavior is captured only uniaxial with the MMM-PM.

## 5.2 Simulation of the Inelastic Behavior of TRC due to Tensile Loading

In the following we consider a so called normal reinforced TRC specimen with coaxial loading and reinforcement directions. After formation of the first matrix crack the rovings are bridging the cracks. In contradiction to the double sided pullout test the amount of rovings is sufficiently high, which leads to further matrix cracks. Figure 16 shows the mesoscopic model.

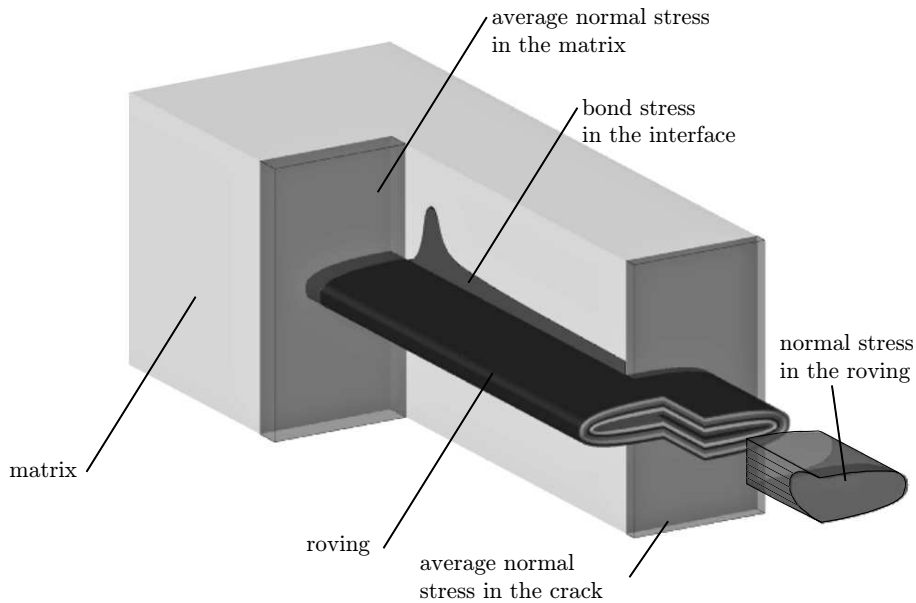


Figure 16. Considered stresses of TRC model on the meso scale

The number of cracks, the crack widths and the crack spacings depend on the transferable shear stress between roving and matrix. According to the determined bond law and the shape of the roving a critical bond length  $L_c$  can be found, which is large enough to lead to a critical stress state within the matrix for further crack development. Therefore the final crack pattern shows a crack spacing between  $L_c$  and  $2L_c$ . If the specimen is very large the mean crack spacing tends to  $1.34L_c$ . But this theoretical mean value is of minor importance to the considered  $200\text{ mm}$  long specimen with an average crack spacing of about  $10\text{ mm}$ . Therefore the bounds for  $L_c$  and  $2L_c$  are calculated for comparison with experimental results, cp. fig. 16.

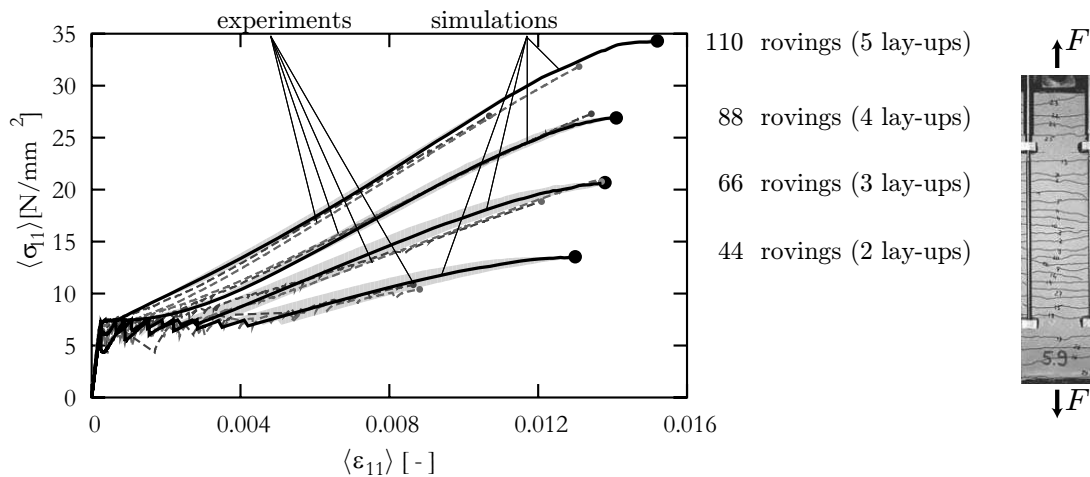


Figure 17. TRC in tension test with varying amount of rovings a) macroscopic stress-strain relation b) picture of the tension specimen with macro crack pattern

Figure 17 shows the predicted behavior of a tension specimen with varying numbers of textile lay-ups. One lay-up (ply) consists of 22 rovings. Increasing the number of lay-ups from 2 to 5 leads to higher ultimate loads combined with changes in the stiffness. The simulation results are plotted as curves for  $L = 1.34L_c$  and an additional shaded areas according its upper boundaries of  $2L_c$  and its lower boundaries of  $1L_c$ .

One important result of the tension test simulation is the influence of the post cracking behavior of the fine grained concrete. In tension tests of steel reinforced concrete this effect is normally neglected, but in TRC the crack bridging over the crack face of the concrete is necessary because of the small crack widths at higher reinforcement percentage. In the case of 2 lay-ups the effective stress-strain response is nearly tri-linear. The elastic part (stage I), the crack developing range (stage IIa) and the final crack opening range (stage IIb) are clearly distinguishable. With increasing number of lay-ups the final macro crack pattern of the TRC specimen is completed at lower

macroscopic strains [Lepenieš (2007)].

The prediction of the ultimate load differs from experimental results. The actual model neglects the scatter of the roving strength in the specimen. Therefore the experimental observed relative rotation of the specimen parts was not simulated during the final failure. The strength of the weakest roving determines the strength of the whole specimen in a tension test, because of the progressive failure process after the first roving breaks.

## 6 Conclusions

The presented hierarchical material model – the Micro-Meso-Macro-Prediction Model (MMM-PM) – of TRC is an assembly of simplified, efficient micro-, meso- and macroscopic models. A micro mechanical analysis simulates the fiber bundle behavior taking the non-uniform stress profile within the roving into account. Based on the derived effective roving model the matrix crack bridging of the rovings is modeled on the meso scale. Additional characteristic model parameters are determined from results of standard pullout tests to simulate the effective macroscopic behavior of TRC for different number of rovings. The presented model predicts the macroscopic material behavior of TRC by means of simulation of the relevant damage and failure mechanisms on the finer resolved scales using homogenization and localization methods for scale transition and scale integration. Results from macroscopic tension tests are used for model validation, whereas the model parameters are determined from independent experimental data.

## Acknowledgments

The authors gratefully acknowledge the financial support of this research from the Deutsche Forschungsgemeinschaft (German Research Foundation) within the Sonderforschungsbereich SFB 528 (Collaborative Research Center) Textile Reinforcement for Structural Strengthening and Retrofitting at Technische Universität Dresden and the support of their colleagues providing all experimental data.

## References

- Eshelby, J. D.: The determination of the elastic field of an ellipsoidal inclusion, and related problems. *Proceedings of the Royal Society of London, A* 241, 376 – 396, (1957).
- Mori, T.; Tanaka, K.: Average stress in matrix and elastic energy of materials with misfitting inclusions. *Acta Metallurgica*, 21, 571 – 574, (1973).
- Lepenieš, I.; Richter, M.; Zastrau, B.: Numerische Simulation des mechanischen Verhaltens von Textilbeton unter Berücksichtigung mehrerer Strukturebenen. In: *Internationales Kolloquium über Anwendungen der Informatik und Mathematik in Architektur und Bauwesen, 10.-12. Juni 2003*, pages 1–12, Bauhaus Universität Weimar (2003).
- Lepenieš, I.; Meyer, C.; Schorn, H.; Zastrau, B.: *Modeling of the Load Transfer Behavior of AR-Glass-Rovings in Textile Reinforced Concrete*. ACI Material – Thin Fiber and Textile Reinforced Cementitious Systems, SP-244CD:15, (2007).
- Lepenieš, I.: *Zur hierarchischen und simultanen Multi-Skalen-Analyse von Textilbeton*. Ph.D. thesis, Technische Universität Dresden (2007).
- Maeder, E.; Plonka, R.: Coatings on alkali-resistant glass fibres for the improvement of concrete. *Journal of Industrial Textiles*, 33(3), 191–207, (2004).
- Böhlke, T.; Brüggemann, C.: *Graphical Representation of the Generalized Hooke's Law*. Technische Mechanik, 21(2):145–158 (2001).
- Richter, M.: *Entwicklung mechanischer Modelle zur analytischen Beschreibung der Materialeigenschaften von textilbewehrtem Feinbeton*. Ph.D. thesis, Technische Universität Dresden (2005).

---

Address: Prof. Dr.-Ing. Bernd W. Zastrau, Institute of Mechanics and Shell Structures, Technische Universität Dresden, D-01062 Dresden.

email: [ingolf.lepenies@tu-dresden.de](mailto:ingolf.lepenies@tu-dresden.de)